Solar Energy Materials & Solar Cells 278 (2024) 113176

Contents lists available at ScienceDirect

Solar Energy Materials and Solar Cells

journal homepage: www.elsevier.com/locate/solmat

Corrosion characteristics of 316L stainless steel in oxide-rich molten solar salt at 600 °C

Srinivasan Swaminathan [a,*], Sumit Kumar [b], Axel Kranzmann [a], Rene Hesse [a], Hennig Goldbeck [a], Andrea Fantin [a]

[a] Bundesanstalt für Materialforschung und -prüfung (BAM), Department of Materials Engineering, Division 5.1 - Microstructural Design and Degradation, Unter den Eichen 87, 12205, Berlin, Germany
[b] German Aerospace Center (DLR), 70569, Stuttgart, Germany

ARTICLE INFO

Keywords:
Molten salt corrosion
Solar salt
Thermal energy storage
Stainless steels
Concentrating solar power

ABSTRACT

An attempt has been made in this work, to observe the influence on alloy aging by the sodium oxide (Na_2O) in solar salt (60 wt% $NaNO_3$ + 40 wt% KNO_3). The accelerated aging was established by adding Na_2O (0.005, 0.07, 0.135 and 0.2 wt%) to the solar salt and their effect on corrosion of 316L stainless steel (SS) at 600 °C in that oxide-rich solar salts for 168 h in synthetic air was investigated. Corrosion is significantly more in oxide-rich solar salt compared to pure solar salt. Strikingly, the oxide scale-base metal interface is wavy in solar salt containing 0.005 % Na_2O clearly shows the oxide addition to salt melt influences Cr-rich inner oxide layer formation and its selective dissolution at early stage that leads to non-uniform corrosion. Interestingly, with increase of Na_2O to 0.07 %, steel corrosion proceeded uniformly by accelerated disintegration of Cr-rich inner layer and subsequent dissolution. Severe scale spallation and weight loss in nitrate melt containing 0.2 % Na_2O fostering more rapid corrosion, alarming that substantial tolerance of oxide content in solar salt is $\geq$ 0.135 % for an acceptable corrosion of 316L SS. Despite preferential dissolution of Cr and scale degradation/spallation with increased oxide content in solar salt, the corrosion layer in all cases comprised of sodium ferrite, and Cr-rich Cr-Fe mixed oxides with the Ni enrichment at the scale-metal interface. Competing processes between oxide scale growth, degradation and dissolution or even spallation has been discussed with an emphasis of Na_2O addition to solar salt.

1. Introduction

Renewable energy technologies are gaining more interest to control global warming and carbon emissions by reducing the use of fossil fuel-based energy sources. The solar energy resource is virtually a clean and unlimited compared to any conceivable future demand for energy. Among the renewable energy technologies, concentrated solar power (CSP) with thermal energy storage (TES) is a promising technology which can enable large-scale penetration of solar power into the electricity grid [1,2]. Indeed, TES is the main advantage of CSP plants, with that electricity can be readily generated at night or even on cloudy days (independent of solar collection), which permits for rapidly dispatchable and/or continuous power, and therefore, commercial investment on the CSP plants is increased in the last decade [3,4]. In CSP installations, the molten nitrate salts, known as 'solar salt', i.e., a non-eutectic salt mixture comprised of 60 wt% sodium nitrate ($NaNO_3$) and 40 wt% potassium nitrate (KNO_3), have widely been used as heat transfer fluid (HTF) and TES media, mainly because the solar salt possessed of high energy density, high heat capacity, low vapor pressure, and cost-effective as well [5–7].

The molten solar salt power tower technology comprises two tank thermal storage design – a cold (290 °C) and a hot tank (565 °C), a cost-effective energy storage system that decouples solar collection from the electricity generation. The carbon steels are in use for cold salt containment as the solar salt's corrosivity is low at 290 °C whereas the hot salt containment components require 300-series austenitic stainless steels to withstand high corrosion at 565 °C [7–10]. To enhance the thermal to electrical conversion efficiency and to decrease the associated electricity cost of CSP plants, operating CSP turbines with high inlet temperatures, instead of $\leq$550 °C, is one possible strategy. Basically, the storage capacity of TES system is proportional to the difference of hot and cold tank temperatures, meaning that more energy can be stored by

* Corresponding author.
E-mail addresses: srinivasan.swaminathan@bam.de, srini.snsharma@gmail.com (S. Swaminathan).

https://doi.org/10.1016/j.solmat.2024.113176
Received 21 May 2024; Received in revised form 11 September 2024; Accepted 14 September 2024
Available online 19 September 2024

increasing hot tank temperature if the cold tank temperature remains constant. Moreover, a small-sized TES system, i.e., a reduced tank volume is achievable by bringing up the large temperature difference between hot and cold tank. But the nitrate salts (solar salts) are restricted in use to 565 °C owing to its chemical stability. Despite solar salt is considered stable in current CSP operating temperatures (290–565 °C), the salt chemistry (or stability) and corrosivity to its containment materials can be affected over time. In fact, multiple thermal decomposition kinetics and complex reactions of molten nitrate salts have already been reported in the literatures [11–15]. Naturally, increasing the service temperature (> 565 °C) brings more challenges in terms of undesired changes in molten solar salt chemistry and amplified corrosion of CSP pipes and tanks containing such liquids at high temperatures.

The chemistry of molten solar salt evolves over time as a result of contact with the cover gas atmosphere and containment materials. Undecomposed molten solar salt constitutes nitrate anions (NO_3^-) and the sodium and potassium (Na^+, and K^+) cations. Numerous publications [11,15,16], reported that thermal decomposition of molten solar salts occurs via two widely accepted critical chemical reactions: (1) decomposition of nitrate ions (NO_3^-) to nitrite ions (NO_2^-), and (2) further decomposition of nitrite ions (NO_2^-) to oxide ions, such as doubly charged single atomic oxide ions (O^{2-}), peroxide (O_2^{2-}) and/or hyperoxide or superoxide ions (O_2^-). It should be noted that the exactness of oxide ions and their formation reaction pathways are not clearly known yet, however, as the stability of nitrite ions are lesser than the nitrate ions, the decomposition of nitrite ions to form oxide ion species is the most probable mechanistic description stated in large number of publications [16,17] and the refs. therein. In addition, importantly at higher temperatures (≥600 °C), the formation of alkali oxides (such as Na_2O, Na_2O_2) from nitrite ions is characterized as third stage possible reactions [16,18,19]. Though increase of service temperatures is positive in-terms of improving the storage capacity of TES systems, and the overall efficiency of CSP plants, but are also negative as the formation of oxide ions aggravate corrosion of salt containment materials.

Despite a good deal of molten alkali nitrates corrosion data have been gathered in the past on a large spectrum of Fe-based and Ni-based alloys [20–26], however, it does not provide a comprehensive understanding of the metallic corrosion processes, reactions, and mechanisms in molten solar salt at temperatures ≥600 °C. As stated briefly in the above paragraph, decomposition reactions intrinsic to molten nitrate salts favor the formation of a variety of other ionic species depending on the temperature and cover gas atmosphere [27–31]. For instance, solar salt in equilibrium with synthetic air yields ~3 wt% of nitrite ion content at 565 °C, and that increased to ~5.5 wt% at 600 °C [21]. At higher temperatures, nitrite ions further decompose into variety of oxide ion species, in particular, 1 mol.% of peroxide ion concentration is estimated in the melt at 630 °C as per the thermochemical equilibrium calculations. It has already been documented that the oxide ions in the molten salt are extremely aggressive which could exacerbate corrosion of the container alloys [19,32]. Therefore, an objective of the present work is, to provide systematic understanding on the role of oxide ions in 316L stainless steel (SS) corrosion at 600 °C which is very important for the advancement of molten nitrate salt-based energy storage technology. In this current work, to better correlate the corrosion processes of 316L SS in extreme conditions of decomposed solar salt with high oxide ion contents, corrosion exposures have been conducted at 600 °C in solar salt containing 0.005–0.2 wt% of Na_2O under synthetic air for 168 h. This approach is novel in a way to provide insight into the long-term corrosion performance of 316L SS at 600 °C in short exposure time itself by mimicking solar salt aging with an intentional addition of the sodium oxides (0.005, 0.07, 0.135 and 0.2 wt%) to 60 wt% $NaNO_3$-40 wt % KNO_3 mixture, i.e., oxide-rich solar salt. Perception of the corrosion layer grown during the early stage of exposure in this synthetically aged oxide-rich or Na_2O-added nitrate solar salt mixtures (representing extreme condition of melt decomposition at ≥ 600 °C) is necessary, which would then infer at lest in part, the accelerated corrosion that structural materials experience in the CSP plants coupled with the TES systems. Indeed, the lab scale experiments to explore early-stage corrosion under accelerated corrosive conditions at ≥ 600 °C are extremely valuable for screening the established as well as the newly developing steel grades for the construction of CSP-TES plant components such as storage tanks, pipes, etc. In the present work, the gravimetric weight-change analysis and characterization of the formed corrosion products on 316L SS exposed to oxide-rich solar salt by means of GI-XRD, SEM-EDX, FIB-EDX are presented. Based on the phase and chemical analysis of corrosion products formed in Na_2O-added solar salt, this work addresses the competing processes between protective oxide layer formation because of solar salt regeneration and aggravated corrosion by oxide layer dissolution. Moreover, understanding corrosion behavior of 316L SS by artificial aging of solar salt with systematic variation of Na_2O (0.005–0.2 wt%) carried out in this work will support the efforts towards pushing the temperature limit imposed by salt decomposition and steel corrosion.

2. Material and methods

2.1. Preparation of oxide-rich solar salts and steel samples

At first, the solar salt (60 wt% $NaNO_3$-40 wt% KNO_3) was prepared by stoichiometric mixing of $NaNO_3$ (Merck, purity >99 %) and KNO_3 (Merck, purity >99 %). Then, four different concentration of sodium oxide (Na_2O) in wt%: 0.005, 0.07, 0.135 and 0.2, were weighed and each of them were mixed separately into the solar salt, to have four different Na_2O-added solar salt mixtures, i.e., oxide-rich solar salts with varied Na_2O (0.005–0.2 wt%). For instance, 0.2 wt%-added solar salt meaning that 99.8 wt% of solar salt has been mixed with 0.2 wt% of Na_2O. The purity of sodium oxide (Na_2O from Alfa Aesar) is 80 %, and ~20 % of Na_2O_2 (sodium peroxide) as an impurity in it, meaning that sodium oxide purchased and labelled as 'Na_2O' from the manufacturer were actually the mixtures of 80% Na_2O and 20% Na_2O_2. It must be noted that all the four different Na_2O-added solar salt mixtures (each one of oxide-rich solar salt weigh 100 g in total), were carefully prepared in the glove box (GS Glovebox System Technik GmbH, Type: Mega-2, O_2 < 0.5 ppm, H_2O < 5 ppm) to avoid contaminations. All the four different oxide-rich solar salt mixtures (0.005, 0.07, 0.135 and 0.2 wt% Na_2O-added solar salt) were separately placed into the well-cleaned and dried alumina crucibles, i.e., an individual crucible for each Na_2O-added solar salt. To remove any trace moisture in the oxide-rich solar salts, all four salt-filled crucibles were further dried overnight at 180 °C.

The samples of dimensions of 20 mm × 10 mm x 3 mm, were cut from the 316L austenitic stainless steel (316L SS) sheets, and ground till P600 grit surface finish using SiC emery papers. Afterwards, the samples were cleaned first in deionized (DI) water, and then in acetone. The actual chemical composition of the 316L SS (in wt.%) measured through the spark emission spectrometer (SPECTROLAB S, AMETEK), is presented in Table 1.

2.2. Corrosion exposures in oxide-rich solar salts

The experiment was conducted using vertical alumina crucibles and a customized convection furnace that has four identical holes for the alumina crucible insertion from the top. Given that solar salt decomposes at higher temperatures and has the potential for salt creeping and salt evaporation outside the alumina crucibles during the experiment, there exists the possibility of a consequential weight change. To prevent creep of the salt out of the experimental set up, the crucibles were positioned to extend approximately 30 mm out of the furnace. A hollow 3D-printed alumina sample holder (with the compartments, to hold up to 10 samples vertically) was used, which allow not only the full immersion of samples in the alumina crucible but also separating the samples, and thereby, avoiding the galvanic corrosion. To improve the accuracy of the results, two parallel steel samples were vertically

Table 1
Chemical composition of 316L stainless steel (wt%) used for this study.

C	Si	Mn	P	S	Cr	Mo	Ni	Co
0.0218	0.520	0.910	0.0355	0.0013	17.10	2.02	9.86	0.207
Cu	**Nb**	**Ti**	**V**	**Ta**	**B**	**N**	**O**	**Fe**
0.485	0.0145	0.0091	0.0652	0.0011	0.0018	0.0485	0.0046	68.60

positioned in the separate compartments of that 3D-printed alumina sample holder. After placing the samples, the holder was positioned at the bottom of the alumina crucible, and then, the crucible was filled with 100 g of Na_2O-added solar salt. In this way, four crucibles were utilized separately with four different oxide-rich solar salt (i.e., 0.005, 0.07, 0.135 and 0.2 wt% added solar salt). The stainless-steel top flange with feedthroughs was used to seal the crucible, allow for well-controlled gas atmosphere with gas inlets and outlets, as well as to ensure temperature control throughout the experiment, an alumina shielded K-type thermocouple submerged in the salt bath was used. The corrosion experiment of 316L SS sample in Na_2O-added solar salt was carried out at 600 °C for 168 h in a flowing synthetic air (Linde, grade 5.0) atmosphere with a flow rate of 100 ml/min. As a reference experiment, corrosion exposure of 316L SS sample in pure solar salt was also carried out, in addition to the four different (0.005, 0.07, 0.135, and 0.2 wt%) Na_2O-added oxide-rich solar salt exposures. The photographs of the experimental set up and the sample holder can be found in Ref. [29]. Before starting molten salt corrosion exposure, all the samples were weighed initially, and their physical dimensions were noted.

2.3. Post-exposure analysis of steel samples

Upon 168 h-completion of the corrosion exposures, the 316L SS samples (labelled as 0.005Na_2O, 0.07Na_2O, 0.135Na_2O, 0.2Na_2O and Ref. exposure (solar salt without Na_2O)) were taken out from the molten salt, air cooled, and washed in DI water to remove the residual salt before weighing. The molten salt corrosion-induced weight change per unit surface area was calculated from the difference between weight measured before and after the corrosion exposure. The X-ray diffraction analysis for phase identification of the corrosion products was carried out, in grazing incidence X-ray diffraction (GI-XRD - Seifert XRD 3000 PTS) configuration. The diffractometer was configured with grazing incident angle of 1.5°, in the 2θ range of 18–80° at a step size of 0.02° with a measuring time of 10 s per step. Using the same measuring conditions, a Si standard diffraction pattern was acquired to ensure correct device calibration. For the qualitative evaluation of the phases in the corrosion products, the Le Bail fitting [33] was performed in TOPAS (TOtal Pattern Analysis Solutions [34]) software with ICSD (Inorganic Crystal Structure Database) input. The measured or observed patterns were then compared to a database of known patterns, which were then used as inputs for qualitative refinements. The surface and cross-sectional morphologies of corrosion products were observed using scanning electron microscopy (SEM - Tescan Vega3), and their elemental analyses were conducted by means of an energy dispersive X-ray spectroscopy (EDX). To carry out cross-sectional analyses of corrosion layer in SEM-EDX, the samples were prepared by cutting and embedding them in an epoxy resin followed by adequate grinding and polishing. Prior to mounting in resin, a layer of Au by sputtering followed by a layer of Ni by electrochemical deposition were done on the samples to avoid damage of the corrosion layer during the preparation of cross-sections. Electrolytic deposition of Ni was carried out in nickel sulfate containing electrolyte bath with an optimized DC current density of ~30 mA/cm^2 maintained between counter electrode (Ni sheet) and the working electrode (sample). The sputter coated Au provides better imaging contrast between the mounting material, Ni layer and corrosion layer, whereas Ni layer provides a protection to the corrosion layer. The reference exposure sample, i.e., a sample exposed to pure solar salt was cross-sectioned using dual beam focused ion beam (FEI FIB Quanta 3D FEG), and subsequently the corrosion layer was analyzed by means of EDX coupled with the FIB. Additionally, the metallographic cross-section was also done for this reference exposure sample and validated with the FIB-EDX cross-section.

3. Results and discussion

3.1. Weight change characteristics

The weight change characteristics of 316L SS samples exposed to four different oxide-rich solar salts (0.005, 0.07, 0.135, and 0.2 wt% Na_2O-added solar salt) or pure solar salt (Ref. exposure) at 600 °C for 168 h in synthetic air are plotted in Fig. 1. The weight changes upon isothermal exposure were measured in units of weight change per unit surface area (mg/cm^2) to monitor the progress of corrosion with Na_2O-variations in solar salt. Despite it's only the qualitative data, but this data provides some insight into the corrosion process. At first, it's clear that weight changes of 316L SS samples are sensitive to Na_2O-concentration in solar salt. As can be seen in Fig. 1, the sample exposed to pure solar salt containing no Na_2O (Ref. exposure) showed the smallest weight gain whereas the samples exposed to 0.07 wt% Na_2O-added solar salt displayed the highest weight gain. There are two possible processes contribute to weight gain upon molten nitrate salt exposure: (1) uptake of oxygen, and sodium from the molten salt environment and oxide layer growth/thickening; (2) healing of the spalled oxide layer or regions. Obviously, the weight loss is due to severe spallation and/or severe dissolution of oxide layer in the salt melt.

Oxide-rich solar salt displayed reasonable weight gain, except the one exposed to 0.2 wt% Na_2O-added solar salt. No spallation of corrosion layer observed in samples exposed to pure solar salt, 0.005, 0.07 and 0.135 wt% Na_2O added solar salts, indicating oxide scale growth is dominant. It must be noted that the intrinsic thermal decomposition of

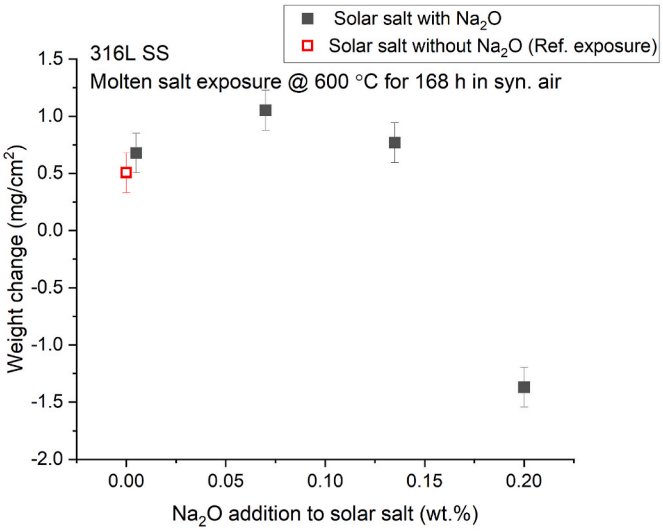

Fig. 1. The weight change behavior of 316L SS samples exposed at 600 °C to oxide-rich solar salts (i.e., solar salt with various concentration of Na_2O) or pure solar salt for 168 h in synthetic air atmosphere. The weight loss observed for a sample tested in 0.2 wt% Na_2O-added solar salt indicates obvious spallation of the corrosion layer.

pure solar salt at 600 °C (i.e., conversion of nitrate to nitrite ions, and nitrite to oxide ions), that generate substantial oxide ions which leads to corrosion and subsequent scale growth, as indicated by the weight gain data. The weight change values with increase of Na_2O-concentration to 0.2 wt% in the solar salt clearly indicate that oxide-rich solar salt has a detrimental effect on the oxide scale dissolution and/or adhesion that aggravates steel corrosion. Additionally, weight loss in 0.2Na_2O sample is likely due to the stress at the oxide-base metal interface, i.e., the stress arises from the mismatch in thermal expansion coefficients between the oxide and base metal can cause scale delamination upon sample cooling [35]. Moreover, the volumetric mismatch during corrosion layer formation could also contribute to scale spallation. Overall, the weight change data evidenced the influence of Na_2O content in the solar salt, particularly, the magnitude of Na_2O effect started showing at 0.07Na_2O sample through weight gain and largely sensitive at 0.2Na_2O sample through weight loss. This will be discussed further in the following section with the surface and cross-sectional micrographs as well as the elemental analysis of the corrosion products in each case.

3.2. Phase analysis of the corrosion layer

The GI-XRD patterns of the corrosion layer formed on 316L stainless steel after exposing to solar salt with various concentration of Na_2O ((a) 0.005, (b) 0.07, (c) 0.135 and (d) 0.2 wt%) at 600 °C for 168 h are depicted in Fig. 2. The Le Bail fit was employed to establish the crystal symmetry and the lattice parameters of the phases present in the corrosion layer. This involves comparing the measured or observed pattern to a database of known patterns, selecting the closest match and qualitatively fit the lattice parameters. The space groups which better fit the data and their respective international numbers are provided in Fig. 2. All the detected and calculated patterns were shifted vertically, i.e., along the vertical axis to enhance the clarity. At first, the GIXRD analysis presented here suggests that the high intense peaks correspond to the sodium iron oxide, i.e., sodium ferrite ($NaFeO_2$) which is clearly a

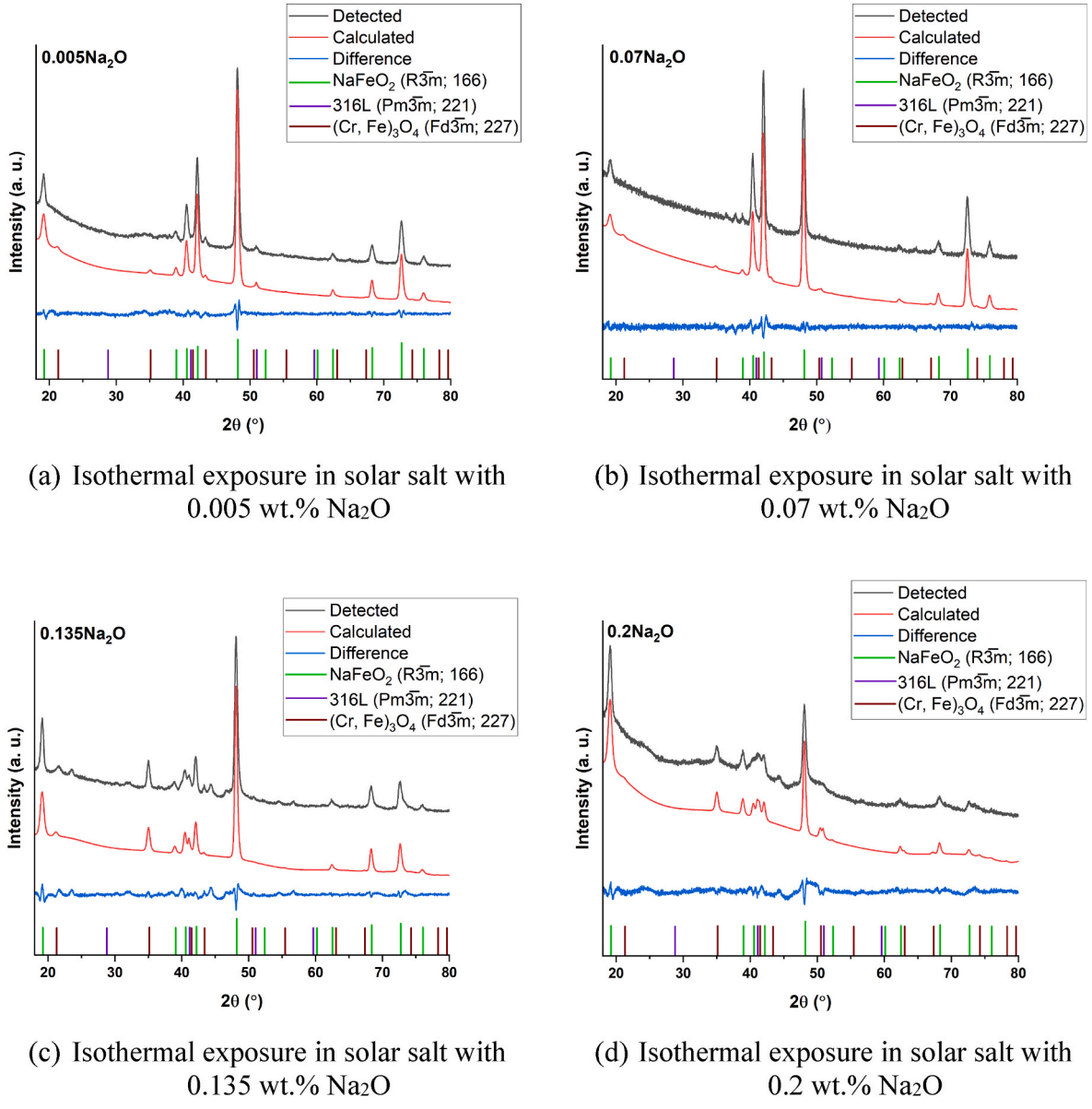

(a) Isothermal exposure in solar salt with 0.005 wt.% Na_2O

(b) Isothermal exposure in solar salt with 0.07 wt.% Na_2O

(c) Isothermal exposure in solar salt with 0.135 wt.% Na_2O

(d) Isothermal exposure in solar salt with 0.2 wt.% Na_2O

Fig. 2. The GI-XRD patterns of 316L SS samples exposed to oxide-rich solar salts (i.e., solar salt with various concentration of Na_2O) at 600 °C for 168 h. The measured data, the calculated data (Le Bail fit using ICSD database input in TOPAS software), and the difference between the two are plotted in black, red, and blue color, respectively, and the patterns are shifted along the vertical axis for the clarity. The reflection positions as per the space groups used for fitting are shown at the bottom vertical lines ($NaFeO_2$ in green, 316L steel matrix in purple, and $(Cr, Fe)_3O_4$ in brown color).

dominant phase of the corrosion layer formed in all Na_2O-added solar salt conditions experimented here. The calculated results, i.e., the Le Bail fit (red color) evidence that most peaks in measured GIXRD data is belong to the trigonal space group R $\bar{3}$m (International number: 166) and lattice parameters which is comparable to the unit cell size of $NaFeO_2$ [36].

Besides the main $NaFeO_2$ phase, a reflection corresponding to (Cr, Fe)$_3O_4$ and/or Fe_3O_4 spinel phase (at 2θ ~43.3°, hkl (222)) as well as a peak (at 2θ ~51°, hkl (111)) from the 316L steel substrate (i.e., γ-Fe) is also found upon exposure in solar salt with 0.005 wt% Na_2O (Fig. 2a). The pattern-matching fit for the (Cr, Fe)$_3O_4$ and/or Fe_3O_4 spinel phase is Fd $\bar{3}$m space group (#227), and the alloy matrix phase belongs to *Pm* $\bar{3}$m space group (#221) [37,38]. As the intensities of the $NaFeO_2$ phase peaks are very high, it can therefore easily be suggested that the sodium iron oxide phase is present at the outer corrosion layer, whereas the Cr-Fe oxide resides in the inner layer. In 0.07 wt% Na_2O case (see Fig. 2b), the doublet peaks (at 2θ ~40.4°, hkl (101) and ~42.1°, hkl (102)) of $NaFeO_2$ phase is relatively high that gives sign of large volume fraction of the sodium iron oxide contribution in the corrosion layer. The striking difference in 0.135 wt% Na_2O (Figs. 2c) and 0.2 wt% Na_2O (Fig. 2d) exposure conditions are the generation of multiple tiny peaks at the doublet regime of $NaFeO_2$ phase, and the emergence of a new peak (at 2θ ~35.1°, hkl (220)) which basically corresponds to the spinel phase (Cr, Fe)$_3O_4$ and/or Fe_3O_4. This discernible change in GIXRD patterns with increase of Na_2O additions (i.e., the increase of spinel phase amount), gives insight into the underlying changes occurs in the formation kinetics of $NaFeO_2$ and/or corrosion layer structures/sequences. Nonetheless, unindexed peaks in Fig. 2c and d indicates the possibility of unknown phase or the presence of crystalline impurity that could not be resolved with the simple qualitative evaluation/pattern indexing carried out in this present work. But it should be noted that all the GIXRD patterns have been acquired using precession angle of 1.5°, basically to mitigate the 316L steel substrate effect. However, an apparent peak for the austenite phase was observed only in 0.005 Na_2O case, and this could relate to its thickness of corrosion layer formed which is smaller than that of 0.07–0.2 wt% Na_2O cases. Note that the non-uniform background in the 0.2 wt% Na_2O case (Fig. 2d) which is contrary to the 0.005–0.135 wt% Na_2O patterns, is likely associated to uneven surface of corrosion layer formed resulting from a strong interaction between the molten salt containing 0.2 wt% Na_2O and 316L steel surface, and this will be detailed in the following section.

In order to differentiate the growth evolution of corrosion products without Na_2O addition in solar salt, the GIXRD indexed patterns of 316L SS sample exposed to pure solar salt, i.e., oxide-free solar salt at 600 °C for 168 h is given in Fig. 3. Despite this reference exposure diffractograms (Fig. 3) has similar features overall as those observed in 0.005 wt % Na_2O case (Fig. 2a), however, a tiny peak (at 2θ ~35.1°) for the spinel phase is found in addition to the steel substrate peak. Owing to the peak intensities, one would expect that sodium iron oxides are the primary outer layer whereas Cr-Fe oxides is likely to be at the sub-surface (or as an inner layer), and this will be explained further in the following section with appropriate evidence. Formation of the sodium containing exterior corrosion layer, i.e., $NaFeO_2$ in oxide-rich and oxide-free solar salt supports the molten salt fluxing process, and this will be further evidenced with the surface and cross-sectional analyses of the corrosion layer. It should be pointed out here that phase depth profile, i.e., oxide layer sequence based on the obtained diffracted signal intensity is depends on the X-ray penetration depth at an incidence angle of 1.5°, meaning that GIXRD is sensitive to the outermost layer formed by the corrosion processes.

3.3. Surface morphology of the corrosion layer

The SE images in Fig. 4a–d, show the surface morphology of the corrosion layer formed on 316L SS samples that were immersed

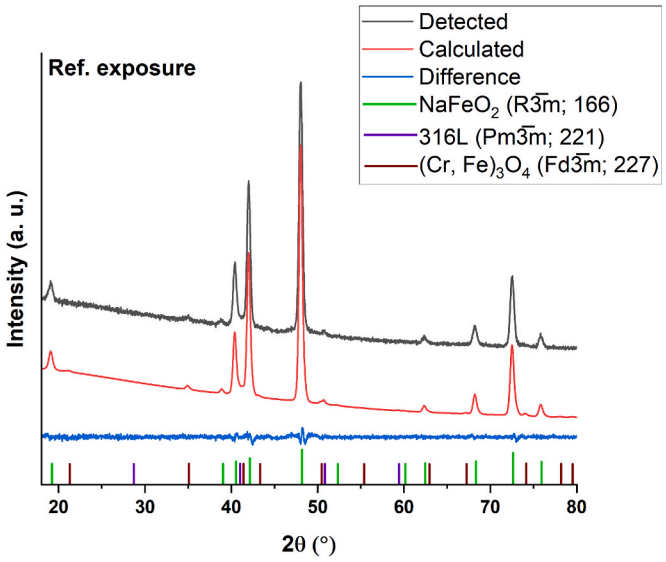

Fig. 3. The GI-XRD characterization of 316L SS sample isothermally exposed to pure solar salt at 600 °C for 168 h, labelled as reference exposure. Similar to Fig. 2, the closely matched space groups (bottom vertical lines) with pattern indexing (including measured and calculated data, and the difference between the two) are presented here in the same format. To display the measured and calculated patterns clearly, the Y-axes limits are extended.

separately in solar salt melt containing different concentration of (0.005, 0.07, 0.135 and 0.2 wt%) of Na_2O. The plan view of the corrosion layer developed upon exposing 316L SS sample to pure molten solar salt (0 wt % of Na_2O, named here as reference exposure) is shown in Fig. 4e. In oxide-free solar salt (Fig. 4e), the corrosion layer surface appears to be covered homogeneously with the numerous faceted (polyhedral and/or tetrahedral) oxide crystallites varied in several microns size. Whereas upon exposure to 0.005 wt% Na_2O-added solar salt (Fig. 4a), the surface oxides turned to be somewhat in irregular shape. Interestingly, the surface exposed to 0.07 wt% Na_2O-added solar salt (Fig. 4b) covered with the flake-shaped oxide crystallites. It must be noted that, surface scale spallation is visible at some spots (see the inset Fig. 4a, b and 4e), even on sample exposed to pure solar salt. This clearly indicates the oxide layer dissolution and spallation characteristics of molten nitrate corrosion, however, the degree of scale dissolution/delamination depends on the aggressivity of molten salt. Despite of dissolution and localized spallation, the weight gain (Fig. 1) observation suggest that oxide growth kinetics is dominant in 0.005 and 0.7 wt% added solar salt exposures. Occurrence of localized bulges or scale buckling (inlay of Fig. 4b) indicates that corrosivity increases with the increase of Na_2O-addition into solar salt. Besides, the volume increase due to oxide scale growth induce substantial compressive stress at the oxide scale-base metal interface and this unbalanced stress should also be accounted for scale spallation. Obvious microstructural differences can be seen in 0.135 wt% Na_2O (Figs. 4c) and 0.2 wt% Na_2O (Fig. 4d) cases. In particular, 0.2 wt% Na_2O-added solar salt case, the corrosion layer surface with fine oxide grains symbolizes that the scale dissolution and delamination dominant here which correlates with the weight loss observation in Fig. 1. The massive scale dissolution and spallation might have altered the topography of corrosion layer formed in high oxide content solar salt melt.

Regardless of the Na_2O-content in solar salt, as a general observation, the EDX elemental mapping analyses of the corrosion layer surface shows an enhanced content of Na, Fe and O existence at the outermost layer (Fig. 5). This correlates well with the GIXRD results (Figs. 2 and 3) that the oxidized surface is primarily composed of sodium iron oxide, and this will also be further evidenced with the cross-sectional analysis of the corrosion layer in the following section 3.4. Increased corrosivity

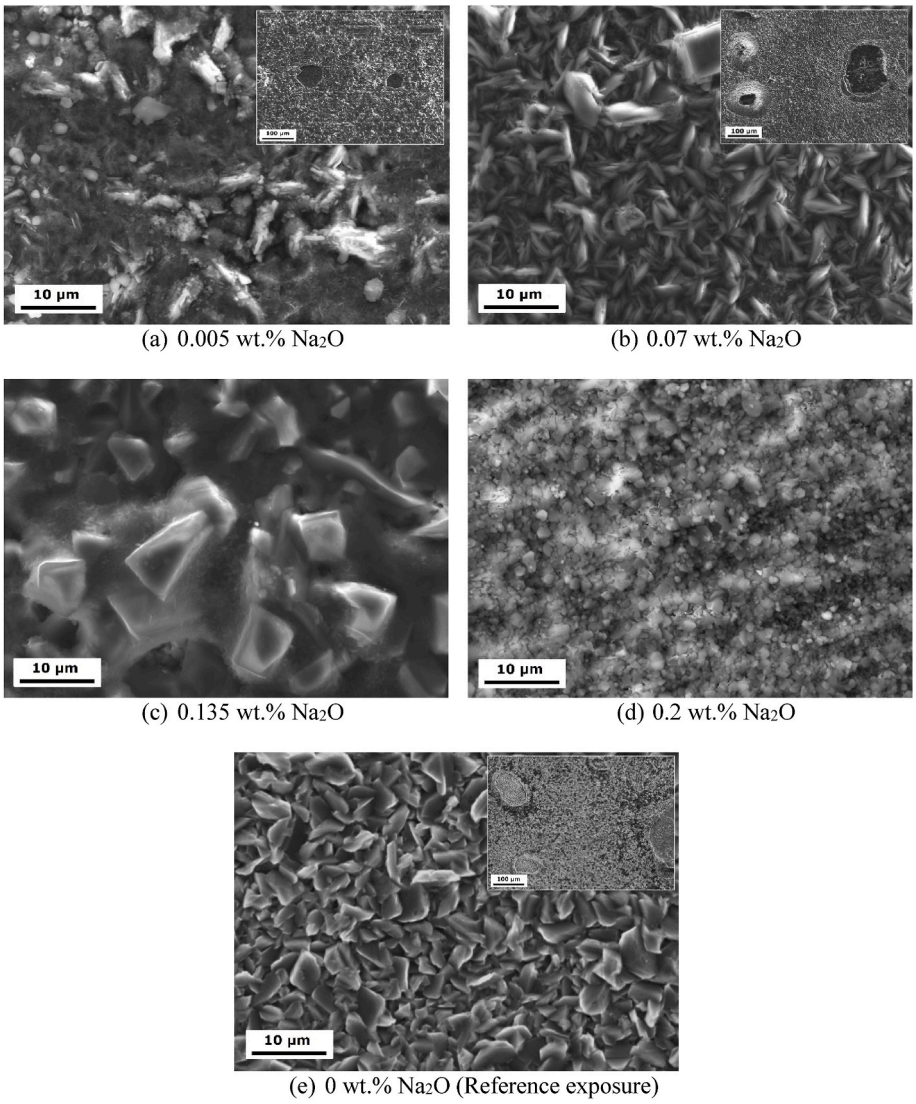

Fig. 4. The SEM surface morphology (SE image) of the corrosion layer formed on 316L SS samples after exposing to different concentration (0–0.2 wt%) of Na_2O-added solar salt at 600 °C for 168 h. The inset low magnification SE images show the spallation characteristics of the corrosion layer.

with an addition of Na_2O to solar salt substantially modifies the corrosion product surface chemistry, and this can be seen in Fig. 5g–i. The presence of Cr in addition to Na, Fe and O at the surface of corrosion layer formed in 0.135 wt% case hinted the coexistence of Cr-Fe-O which is in accordance with the GIXRD results (Fig. 2c). This implies that the complex phase composition is simulated by scale dissolution pronounced kinetics in high oxide content salt melt.

3.4. Cross-sectional analysis of the corrosion layer

The cross-section of 316L SS samples after exposing to each oxide-rich solar salt separately (such as 0.005, 0.07, 0.135, and 0.2 wt% added solar salt), and/or pure solar salt (Ref. exposure with no addition of Na_2O)) were metallographically prepared to observe the elemental constituents and structure of corrosion layer. Figs. 6–9 show the SEM cross-sectional morphologies of the formed corrosion layer in each case and the corresponding EDX elemental mappings of $0.005Na_2O$, $0.07Na_2O$, $0.135Na_2O$ and $0.2Na_2O$ samples.

Cross-sectional examination of the corrosion layer on 316L SS tested with 0.005 wt% Na_2O-added solar salt revealed that formed corrosion layer (see Fig. 6a) is quite adherent, having double layer structure and importantly, not damaged/altered with the metallographic preparation processes. Based on the previous report [20], duplex structured corrosion layer appears to be characteristics of oxide layer formed on all Fe-Cr-Ni austenitic steels at temperatures up to 600 °C. This dual-layer characteristics can be clearly distinguishable (dark and grey contrast) and labelled at high magnification SEM-BSE image shown in Fig. 6b. The EDX elemental mappings of the corrosion layer, and the underlaying steel matrix, is given in Fig. 6c–g. The Au map in Fig. 6h marks the outermost surface of the corrosion layer and most importantly, it confirms that the corrosion products were not damaged in the preparation processes of metallographic cross-section of the corrosion layer. The 316L SS sample tested with 0.005 wt% Na_2O-added solar salt was found to have two primary layers: sodium-iron oxides or sodium ferrite ($NaFeO_2$), and Cr-rich Cr-Fe mixed oxides. The outer layer (dark contrast layer at top) consists primarily of the sodium iron oxide as identified by GI-XRD presented in Fig. 2a, and this evidencing that the GIXRD is sensitive to the outermost layer formed by the corrosion processes. It must be noted that outer sodium ferrite ($NaFeO_2$) layer could also contain some structurally very similar sodium chromium oxide, i.e., sodium chromite ($NaCrO_2$) phase, however, the EDX chemical analysis primarily confirms the sodium iron oxide in corrosion layer structures despite the sodium chromium oxide is also a thermodynamically favorable phase [39,40]. The inner layer is a spinel of Cr and Fe, appears

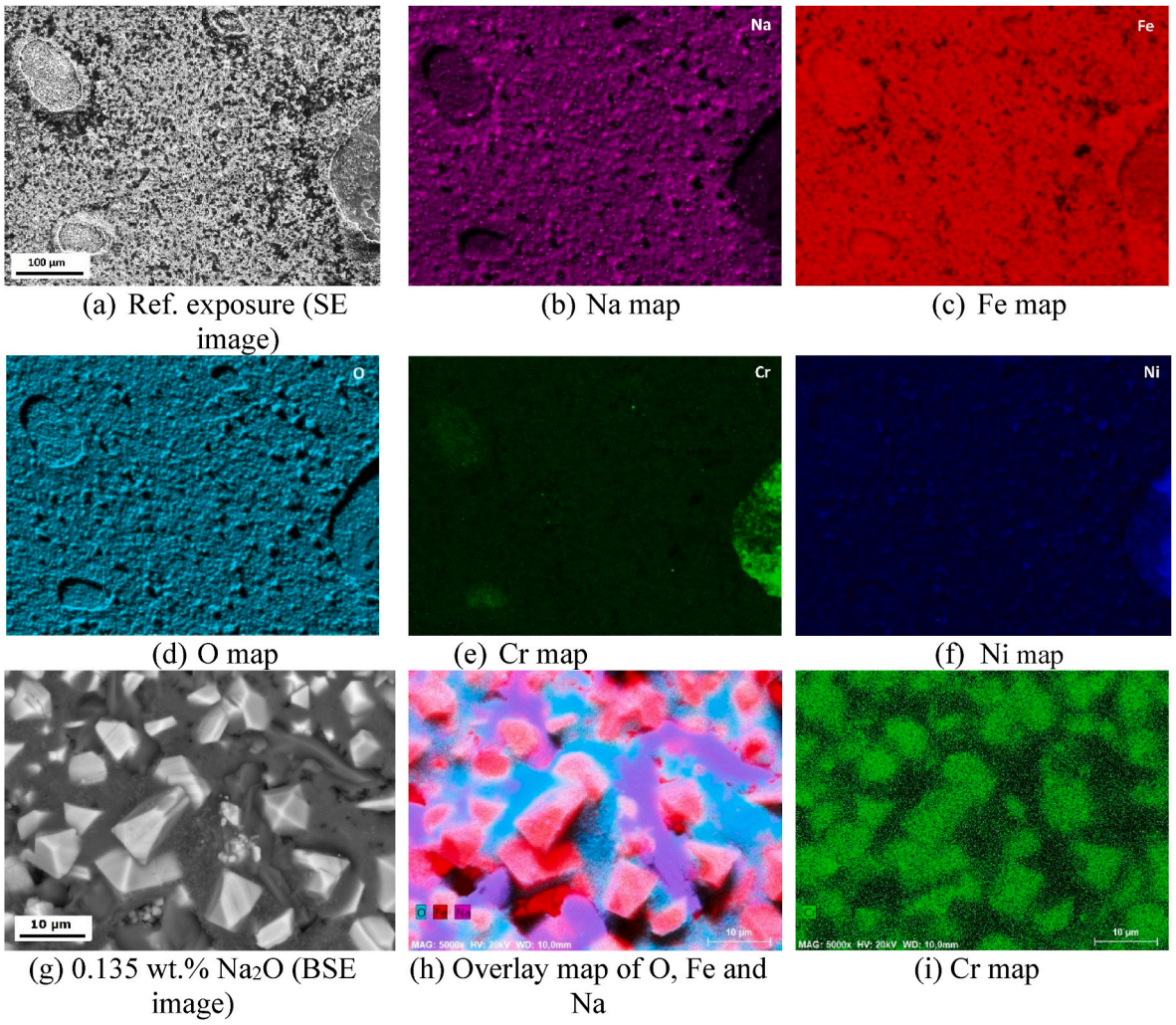

Fig. 5. (a–f) SE image and the corresponding EDX elemental mappings of a corrosion layer surface obtained on 316L SS sample after exposing to pure solar salt (i.e., no Na_2O addition) at 600 °C for 168 h, (g–i) BSE image and the corresponding EDX maps of the corrosion layer surface obtained on 316L SS sample after exposing to solar salt containing 0.135 wt% Na_2O. Elemental maps indicating that outermost corrosion layer constitutes Na, Fe and O, significantly. The Cr map of 0.135 wt% Na_2O case evidencing the heterogenous chemistry of the surface oxide layer in addition to the existence of sodium iron oxides.

to be a Cr-rich spinel oxide that provides the protective layer to some extent regarding corrosion, however, depletion of Cr from the base steel and the enrichment of Ni at the oxide-metal interface can be clearly seen (see Fig. 6f and g). The wavy oxide-metal interface indicates that steel corrosion is influenced by the addition of 0.005 wt% into the solar salt which showed the early stage of Cr-rich layer breakdown with grooving effect at the interface. Grooving interface concludes the high corrosiveness of oxide addition which is basically associated with the area where dissolution/breakdown of the Cr-rich inner layer occurred that allowed molten nitrates to penetrate inward to form the Na-containing product at the oxidation front, however, this can not be considered as an internal corrosion by the salt flux. The dissolution of chromium oxide might have occurred through basic reaction pathway as the basicity of solar salt is increased with 0.005 % Na_2O addition. This means the concentration of oxide ion (O^{2-}) plays a major role on corrosion in oxyanion based molten salts, i.e. metal oxide reacts with the oxide ion to generate metal oxide anion which is soluble in salt [41]. In 0.005 % Na_2O-added salt, the excess oxide ions react with chromium oxide through the following reaction and create the chromate anion, which is highly soluble in the molten nitrates,

$$Cr_2O_3 + O^{2-} + 3/2\ O_2 \leftrightarrow 2CrO_4^{2-} \quad (1)$$

It is well known that element which has more negative Gibbs free energy of oxide formation are highly prone to corrosion. It must be considered that Cr possess more negative free energy to form oxide than Fe and Ni [42], and that clearly reveals the solubility of Cr-oxide in the nitrate melt is higher than that of oxides of Fe and Ni [21]. Similarly, it has also been reported that Cr, Fe and Ni suffer from active dissolution in the molten fluoride salt, with a corrosion resistance order of Cr < Fe < Ni [43,44]. In the present scenario, the redox chemistry of the Na_2O-added solar salt melt reflects the strong oxidizing properties of the melt, so that chromia is not stable in the melt but dissolved as chromates. Thus, the Cr depletion (see Fig. 6f) is strongly attributed to the outward leaching of Cr through the chromate formation as stated in the above chemical equation which in turn resulted in enrichment of Ni at the oxide scale-base metal interface. Interestingly, even in high temperature water environments, 300-series stainless steels are reported to have Ni-enrichment near the scale-metal interface due to Cr-depletion because of Cr-rich inner layer formation in the corrosion scale microstructures [45,46]. This means Ni is not really participated in the oxidation process and obviously concentrated as a compensation effect beneath the inwardly moving oxidation front. As stated above, failure in Cr-rich inner layer resulted in grooving effect (i.e., wavy scale-metal interface) which implies the impact of oxide-rich solar salt on steel corrosion, and the dominant phase boundary reaction kinetics even at this low oxide content (0.005 %) in solar salt.

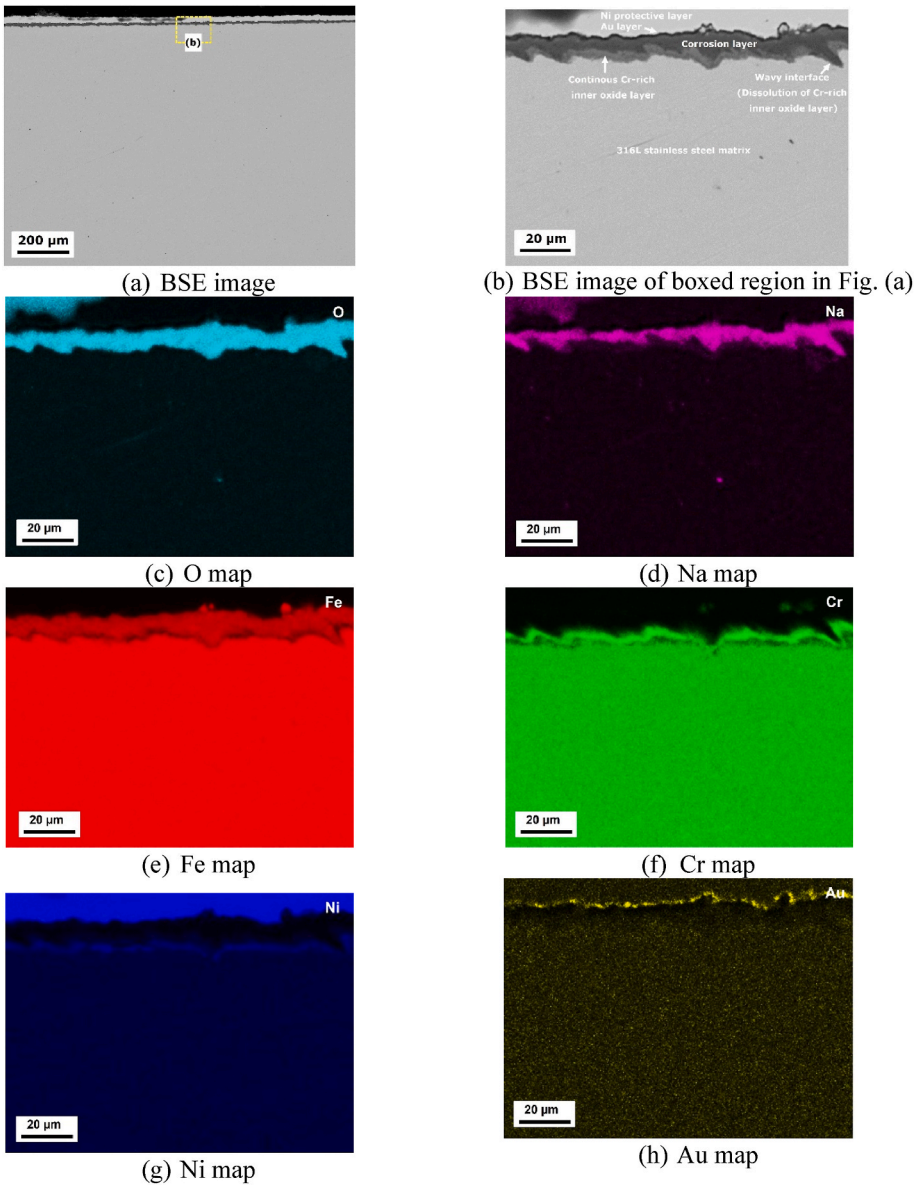

Fig. 6. The SEM cross-sectional morphology and EDX elemental maps of the corrosion layer formed on 316L SS sample after exposing to 0.005 wt% Na_2O-added solar salt at 600 °C for 168 h; (a) low magnification BSE image, (b) enlarged BSE image of boxed region in Fig. 6(a)–and (c–h) the corresponding EDX elemental maps of O, Na, Fe, Cr, Ni and Au, respectively. Dark contrast region within the corrosion layer strongly matches to sodium iron oxide phase. The Cr-depletion and wavy oxide-steel matrix interface with Ni-enrichment assess the impact of Na_2O-addition into the solar salt.

Fig. 7 displays the cross-sectional morphology of the corrosion layer formed in 0.07 wt% Na_2O-containing solar salt melt. Disintegration of Cr-rich inner oxide layer leads to loose and porous appearance, not quite a compact or continuous inner layer as observed in 0.005Na_2O case. The corrosion layer is thicker which is well agree with the weight gain data, but it does not appear as a compact dense scale. Despite of localized surface scale bulging and spallation at some spots in 0.07 wt% Na_2O-added solar salt as identified in Fig. 4b, by correlating weight change data (Fig. 1) and cross-sectional SEM-EDX analysis (Fig. 7) signifying that weight gain was most likely due to thicker sodium iron oxide layer formation. The Cr-rich inner layer that was formed as inner layer in 0.005Na_2O case apparently disintegrated in 0.07Na_2O case. It should be noted that Cr-metal to chromate formation is also possible as per the following equation [47],

$$2Cr + 7NO_3^- \leftrightarrow 2CrO_4^{2-} + NO_2^- + NO \quad (2)$$

By considering the scale thickness it can be stated that Cr is rapidly dissolved whereas iron as well as Ni seems negligibly soluble in this oxide-rich salt melt. Despite the solubility of Cr in the solar salt is quite high, however, the dissolution of Cr into the melt must be kinetically controlled by the diffusion through the outer sodium iron oxide layer. This meaning that the externally formed sodium ferrite ($NaFeO_2$) with increase of Na_2O addition from 0.005 to 0.07 wt% in solar salt is not a protective layer, and this non-protective behavior of sodium-iron-oxide is well in agreement with the previous report [21]. The wavy oxide-base metal interface formed at 0.005Na_2O sample and relatively uniform interface formed at 0.07Na_2O sample, indicating the transition stage of corrosion kinetics. Inward flux of O and Na from the melt is dominant in 0.005Na_2O case whereas the synergy between outward flux of Cr and Fe (or Cr dissolution into the melt), and inward permeability of Na and O, is rate controlling in 0.07Na_2O case. The GI-XRD intensities (Fig. 2b), weight gain data (Fig. 1) and the elemental maps (Fig. 7b–d) are evidencing the transitioning stage of corrosion in 0.07Na_2O sample.

Increasing the oxide content to 0.135 wt% in solar salt leads to an

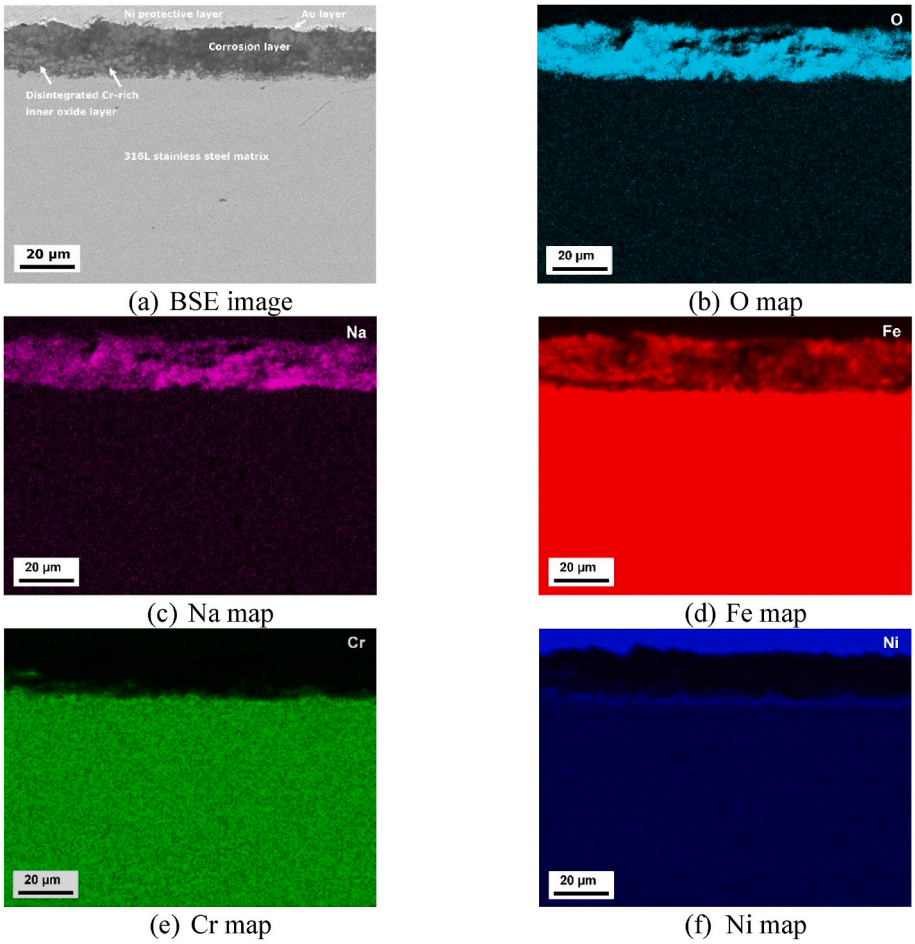

Fig. 7. (a) The SEM-BSE cross-sectional morphology and the corresponding EDX elemental maps of the corrosion layer obtained after exposing 316L SS sample to 0.07 wt% Na_2O-added solar salt at 600 °C for 168 h. Disintegration of Cr-rich oxide layer and formation of relatively dominant $NaFeO_2$ layer indicating the transition stage corrosion kinetics in 0.07Na_2O sample, i.e., uniform alloy corrosion, no grooving interface.

initial stage undulation at the oxide-base metal interface. The overall chemical structure of corrosion layer is same: sodium iron oxide as an outer layer and Cr-rich Cr-Fe spinel oxide as an inner layer with the Ni enrichment at the interface, and this cross-sectional morphology with the corresponding elemental maps are shown in Fig. 8a–e. Despite the corrosion layer is adherent, compact and non-porous, however, a slightly decrease in weight gain data (Fig. 1) indicates that dissolution of corrosion products takes place to some extent in this case. The relative intensities of $NaFeO_2$ peaks in GIXRD, weight gain data and the cross-sectional corrosion layer morphology implies that corrosion layer is affected with the increase of oxide content (0.135 wt% Na_2O) in solar salt, meaning that dissolution kinetics start dominating here. When the oxide content in solar salt exceeds 0.135 wt%, corrosion product dissolution and spallation is a dominant process. Major changes that include accelerated aging and unstoppable steel corrosion occurred at 0.2 wt% Na_2O case. The BSE image in Fig. 8f–j reveals that the corrosion layer is composed of two distinct regions separated clearly by their contrast. The top oxide layer formed at the salt melt-oxide scale interface (adjacent to Au layer; dark in contrast) and the bottom oxide layer at the oxide scale-base metal interface (light in contrast) are very irregular in thickness. In particular, the considerable variability in outer layer thickness or somewhat wavy patterned oxide surface strongly evident that corrosion layer obtained in Fig. 8f is not a first-generation oxide scale, meaning the occurrence of severe spallation. Moreover, observation of fine grained and somewhat rough surface morphology of the corrosion layer (see Fig. 4d) is attributed to accelerated corrosion with an increase of Na_2O content to 0.2 wt% in the solar salt. Similarly, the wavy interface also reflects the lack of adherence, and this can be further evidenced with the weight loss observation in Fig. 1.

Correlating cross-sectional observation of the corrosion layer, the obtained weight gain data and the measured GIXRD patterns confirming that 316L SS sample corroded quite rapidly in the oxide-rich solar salt (containing 0.2 wt% Na_2O) at 600 °C, emphasizing that Na_2O exceeds 0.135 wt% in the solar salt significantly aggravated the corrosion of 316L SS. As reported in the recent studies [48,49], corrosion processes in molten nitrates at or above 600 °C are complex and highly vary upon various factors including overlaying atmosphere and salt impurities/additives, if any. In the present work, increase of Na_2O in solar salt up to 0.2 wt% resulting in high concentration of oxide ions (O^{2-}), and naturally, the basicity of molten nitrates increases with abundance of O^{2-}. It must be noted that basic species present in Na_2O-added solar salt is not necessarily be the single atomic oxide ions (O^{2-}), existence of peroxide (O_2^{2-}) and/or hyperoxide or superoxide ions (O_2^-), is highly possible in accordance with the following reactions [50,51],

$$NO_3^- + O^{2-} \leftrightarrow NO_2^- + O_2^{2-} \quad (3)$$

$$2NO_3^- + O_2^{2-} \leftrightarrow 2NO_2^- + 2O_2^- \quad (4)$$

In fact, under the flowing synthetic air atmosphere here, the superoxide ions (O_2^-) can also be formed,

$$O_2^{2-} + O_2 \leftrightarrow 2O_2^- \quad (5)$$

Also, the reaction between iron oxides and sodium to form sodium ferrites, i.e., sodiation reaction is highly favorable not only in the Na_2O-

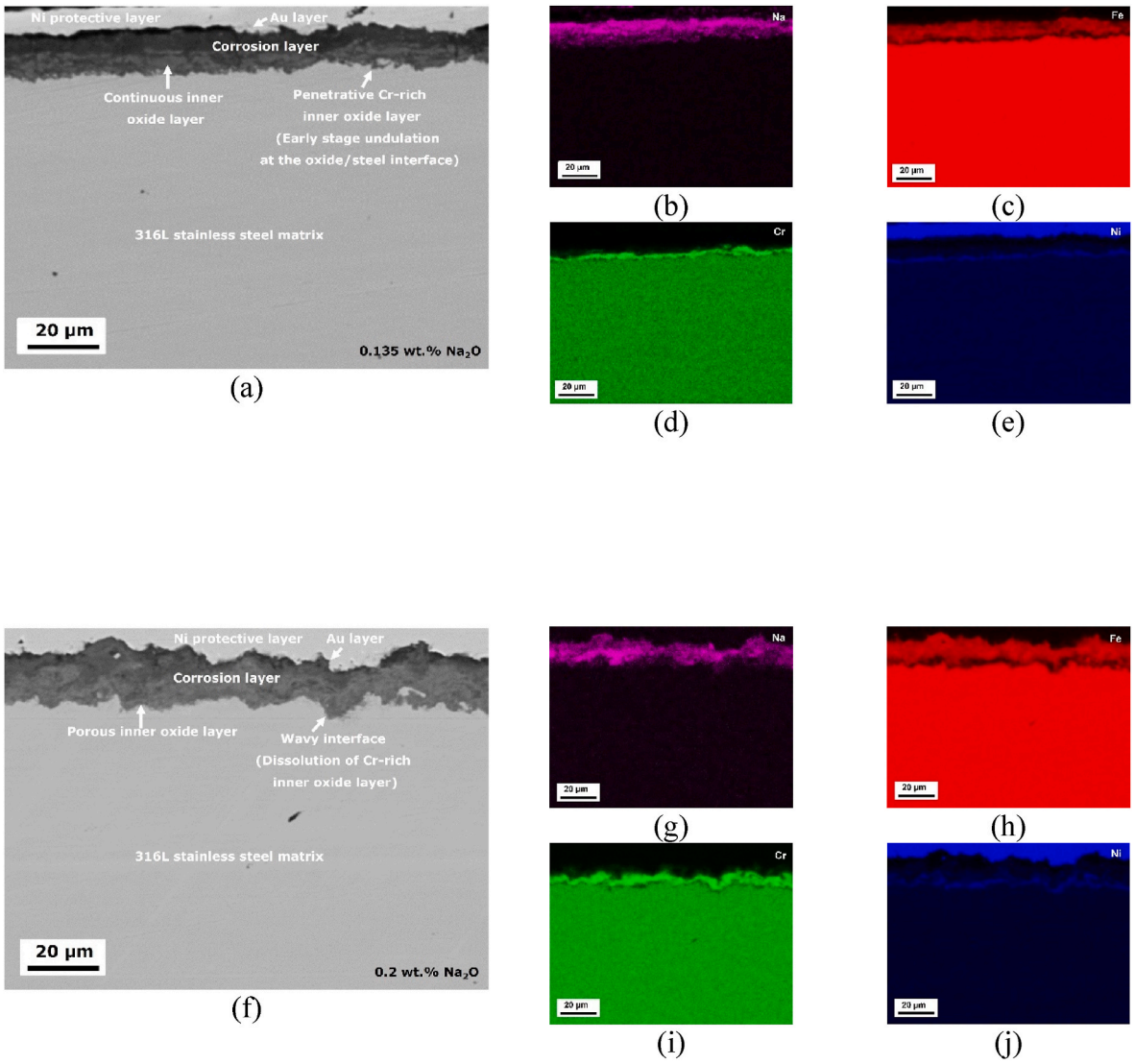

Fig. 8. Cross-sectional SEM-EDX analysis of the corrosion products obtained after exposing 316L SS samples for 168 h at 600 °C in 0.135 wt% Na_2O-added solar salt (a–e) and in 0.2 wt% Na_2O-added solar salt (f–j) for the same duration and temperature. Dark contrast region of outer corrosion layer well relates to sodium iron oxide phase, whereas light contrast region represents the Cr-rich inner oxide layer. Enrichment of Ni at the oxide-steel interface can also be clearly seen.

containing solar salt, but also in pure solar salt at higher temperatures,

$$Na_2O + Fe_2O_3 \leftrightarrow 2NaFeO_2 \quad (6)$$

Though the sodium ion integrates into the corrosion product as per the equation (6), generally the corrosion mechanism is strongly influenced by the anion species of the salt, i.e., oxyanionic ion or simply oxide ion as explained before [41]. Thus, the excessive oxyanion present in the oxide-rich solar salt containing 0.2 wt% Na_2O reacts with metal oxides, chromia and generate metal oxide anion (chromate ion, CrO_4^{2-}) which is soluble in the molten nitrates. Dissolution of corrosion product by salt aggressivity, also the scale spallation reasoning the biggest weight loss in 0.2Na_2O case.

To distinguish the effect of sodium oxide additions on corrosion severity, the cross-sectional analysis of corrosion layer formed on 316L SS upon exposure to oxide-free solar salt (i.e., pure solar salt, named here as reference exposure) at 600 °C for 168 h in synthetic air atmosphere has been conducted. The BSE-SEM image (Fig. 9a) and the corresponding EDX elemental maps of FIB-milled cross-section through oxide layer and underlying base metal (Fig. 9c–h) confirms that an alkali-rich outer oxide scale (i.e., sodium iron oxide) and an inner oxide layer enriched with Cr at the oxide-base metal interface. At the base metal subscale zone, depletion of Cr and enrichment of Ni is obvious. Fig. 9 also validates the cross-section of a corrosion layer accomplished by metallographic method. The cross-section of corrosion layer by FIB cut (Fig. 9a) and metallography (Fig. 9b – low and high magnification image) indicates that the formed corrosion layer in oxide-free salt melt is overall compact with some discontinuities and pores at the inner Cr-rich layer. Despite of small undulation at the oxide-base metal interface at some places, no obvious interfacial grooving, and/or adhesion issues in oxide-free solar salt condition. However, strikingly, the corrosion layer thickness in pure solar salt exposure is much smaller than that of exposures carried out in Na_2O-added solar salt melts (Fig. 10). Overall, the cross-sectional analysis of the corrosion products presented in this work showed that the steel corrosion increased as the Na_2O content increased in the solar salt, notably, at or above 0.135 wt% Na_2O level, the dissolution of Cr, and spallation of the corrosion layer is dominant which clearly confirming the accelerated aging of solar salt and their effect on steel corrosion. This implies the threshold level of oxide addition, above which oxide-rich solar salt significantly aggravated corrosion of 316L stainless steel. It is worthy of study further by including systematic analysis of molten salt chemistry over time, also the corrosion tests with an addition of sodium peroxide in solar salt.

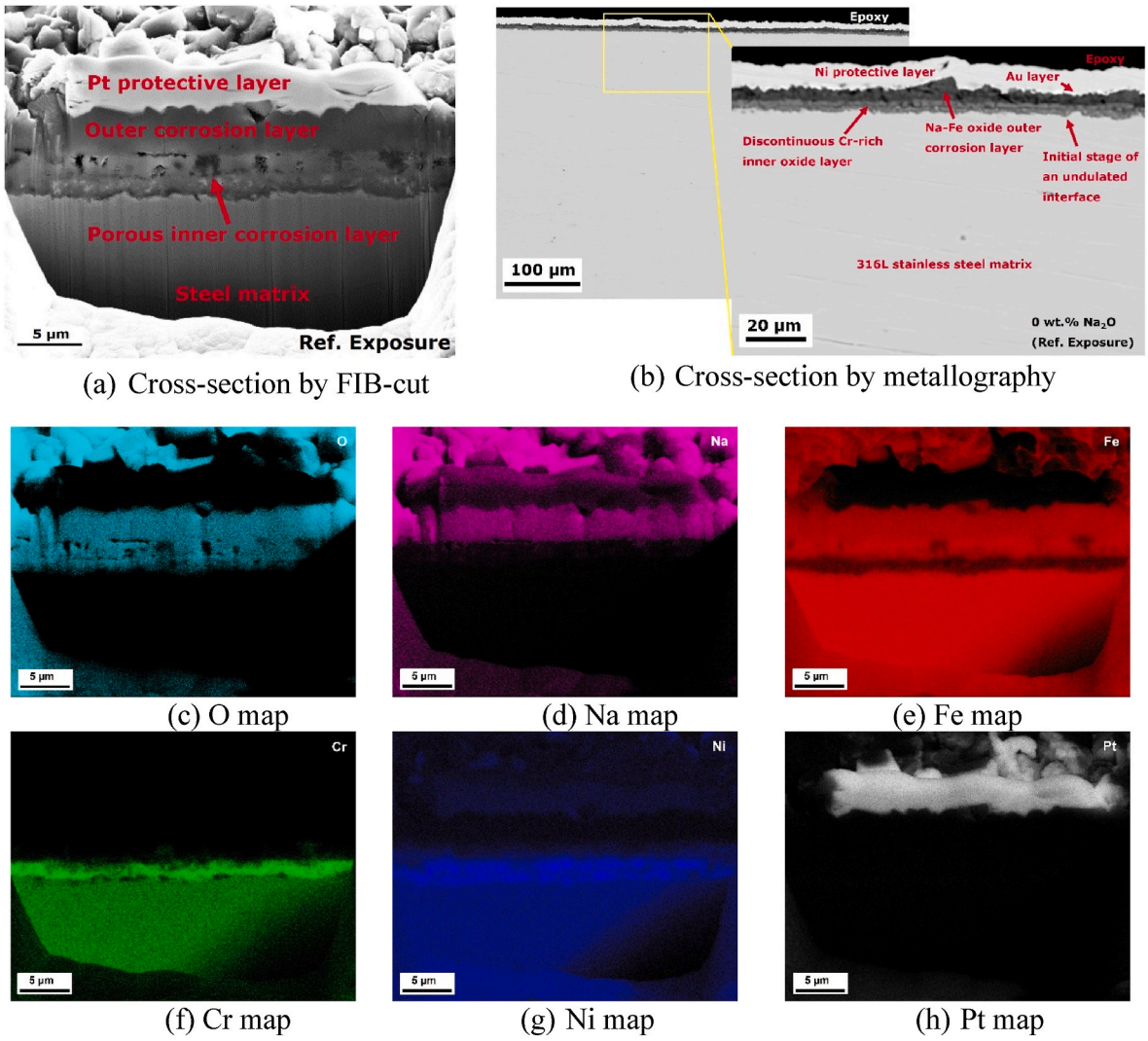

Fig. 9. FIB-cut and metallographic cross-sectional analysis of the corrosion product obtained after exposing 316L SS sample for 168 h at 600 °C in solar salt; (a) BSE image of cross-section by FIB-cut, (b) BSE images of cross-section by metallography at low and high magnifications, (c–g) EDX elemental maps of the area corresponding to FIB-cut cross-section shown in Fig. 9(a). Enrichment of metallic Ni at the oxide-steel interface as well as within the inner Cr-rich oxide layer can be recognized.

4. Conclusions

Corrosion exposures in pure and 0.005–0.2 wt% Na_2O-added solar salt demonstrated that oxides in molten nitrate salt has a significant effect on corrosion progresses of 316L stainless steel at 600 °C. The corrosion products observed were predominantly oxides of sodium and iron at the oxide-salt melt interface while inner oxides were mostly Cr-rich Fe-Cr spinel oxides $(Cr, Fe)_3O_4$ and/or mixtures of Cr-rich Fe, Cr and Ni oxides with consistent Cr depletion and Ni enrichment at the oxide scale-base metal interface. Sodium iron oxide (i.e., sodium ferrite, $NaFeO_2$) is the dominant corrosion product formed on the outer corrosion layer regardless of the oxide content in the solar salt. The wavy-like or grooving oxide scale-base metal interface in oxide-rich solar salt is directly related to failure of Cr-rich inner layer by selective dissolution possibly along the grain boundaries of the underlaying metal, confirming that Cr_2O_3 or Cr-rich inner layer does not play a role of a protective layer which resulted in corrosion progresses. As the basicity of solar salt is increased with 0.005 % Na_2O addition, the abundance of oxide ions react with an initially formed chromium-rich inner oxide and create soluble chromate anions which explains the selective dissolution of chromium oxide and subsequent grooving at the scale-metal interface. The gravimetric weight change characteristics, median thickness of formed corrosion layer measured from the cross-sectional analyses imply that corrosion occurred by oxide growth dominant in solar salt containing 0, 0.005 and 0.07 wt% Na_2O whereas the dissolution and spallation are dominant processes at 0.135 and 0.2 wt% Na_2O-added solar salts. The dissolution and spallation tendency of corrosion layer depended on the concentration of Na_2O-added into the solar salt and such tendency was exacerbated relatively at or above 0.135 wt% of Na_2O. This implies the threshold level of oxide addition, above which oxide-rich solar salt significantly aggravated corrosion of 316L stainless steel at 600 °C, clearly evidencing the effect of solar salt aging, in particular, role of oxide ions on steel corrosion at elevated temperatures.

CRediT authorship contribution statement

Srinivasan Swaminathan: Writing – review & editing, Writing – original draft, Visualization, Project administration, Methodology, Investigation, Formal analysis, Data curation, Conceptualization. **Sumit Kumar:** Writing – review & editing, Methodology, Investigation, Data curation, Conceptualization. **Axel Kranzmann:** Writing – review & editing, Formal analysis, Conceptualization. **Rene Hesse:** Investigation, Data curation. **Hennig Goldbeck:** Investigation, Data curation. **Andrea Fantin:** Writing – review & editing, Formal analysis, Data curation.

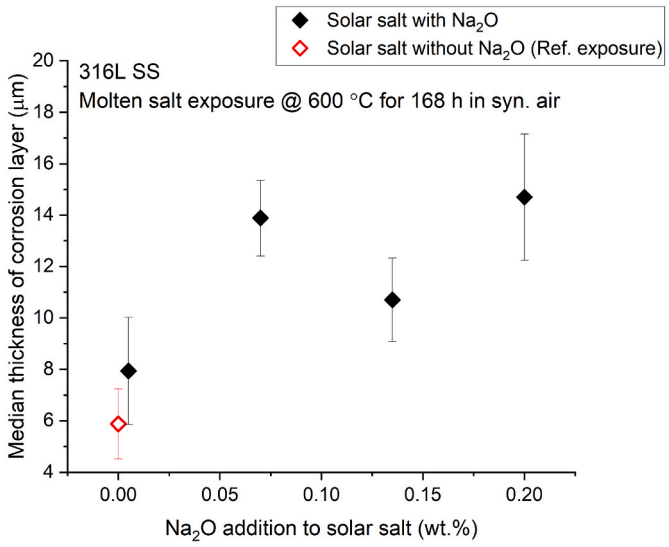

Fig. 10. The median thickness of corrosion layer formed upon exposing 316L SS samples to oxide-rich solar salts (i.e., solar salt with various concentration of Na_2O) and pure solar salt at 600 °C for 168 h in synthetic air atmosphere.

Declaration of competing interest

The authors declare the following financial interests/personal relationships which may be considered as potential competing interests:

Srinivasan Swaminathan reports financial support was provided by Deutsche Forschungsgemeinschaft (DFG) - German Research Foundation. Sumit Kumar reports financial support was provided by Deutsche Forschungsgemeinschaft (DFG) - German Research Foundation. If there are other authors, they declare that they have no known competing financial interests or personal relationships that could have appeared to influence the work reported in this paper.

Data availability

Data will be made available on request.

Acknowledgements

Grateful thanks are expressed to the Deutsche Forschungsgemeinschaft (DFG) – the German Research Foundation - project number 455432503, for the funding (grant numbers: STE 1925/5-1, BO 5213/1-1, KR 1999/38-1) through the project “Materials Degradation Phenomena of High Temperature Alloys by Molten Salts (MaDMoS)”. The authors thank Prof. C. Stephan-Scherb, Dr. A. Bonk, and Prof. U. Krupp for the funding acquisition. Gratitude is also extended to Mrs. M. Buchheim, Mr. R. Saliwan and Mrs. G. Oder for their support with the lab facilities introduction. Special thanks to Mrs. H. Strehlau for her timely help with the compositional analysis of 316L SS sample using spark emission spectrometer.

References

[1] P. Denholm, M. Mehos, Enabling Greater Penetration of Solar Power via the Use of CSP with Thermal Energy Storage, National Renewable Energy Laboratory, 2011. Technical Report NREL/TP-6A20-52978.

[2] A.G. Fernández, J. Gomez-Vidal, E. Oró, A. Kruizenga, A. Solé, L.F. Cabeza, Mainstreaming commercial CSP systems: a technology review, Renew. Energy 140 (2019) 152–176, https://doi.org/10.1016/j.renene.2019.03.049.

[3] L.A. Weinstein, J. Loomis, B. Bhatia, D.M. Bierman, E.N. Wang, G. Chen, Concentrating solar power, Chem. Rev. 115 (2015) 12797–12838, https://doi.org/10.1021/acs.chemrev.5b00397.

[4] S. Kuravi, J. Trahan, D.Y. Goswami, M.M. Rahman, E.K. Stefanakos, Thermal energy storage technologies and systems for concentrating solar power plants, Prog. Energy Combust. Sci. 39 (2013) 285–319, https://doi.org/10.1016/j.pecs.2013.02.001.

[5] T. Bauer, N. Pfleger, D. Laing, W.-D. Steinmann, M. Eck, S. Kaesche, High temperature molten salts for solar power application. Molten Salts Chemistry, Elsevier, 2013, pp. 415–439, https://doi.org/10.1016/B978-0-12-398538-5.00020-2.

[6] K. Vignarooban, X. Xu, A. Arvay, K. Hsu, A. Kannan, Heat transfer fluids for concentrating solar power system - a review, Appl. Energy 146 (2015) 383–396, https://doi.org/10.1016/j.apenergy.2015.01.125.

[7] R.W. Bradshaw, D.B. Dawson, W. De la Rosa, R. Gilbert, S.H. Goods, M.J. Hale, P. Jacobs, S.A. Jones, G.J. Kolb, J.E. Pacheco, M.R. Prairie, H.E. Reilly, S. K. Showalter, L.L. Vant-Hull, Final Test and Evaluation Results from the Solar Two Project, Sandia National Laboratories, 2002. Report No. SAND2002-0120.

[8] A. Gomes, M. Navas, N. Uranga, T. Paiva, I. Figueira, T.C. Diamantino, High-temperature corrosion performance of austenitic stainless steels type AISI 316L and AISI 321H, in molten Solar Salt, Sol. Energy 177 (2019) 408–419, https://doi.org/10.1016/j.solener.2018.11.019.

[9] A.S. Dorcheh, R.N. Durham, M.C. Galetz, Corrosion behavior of stainless and low-chromium steels and IN625 in molten nitrate salts at 600 °C, Sol. Energy Mater. Sol. Cells 144 (2016) (2016) 109–116, https://doi.org/10.1016/j.solmat.2015.08.011.

[10] M. Walczak, F. Pineda, Á.G. Fernández, C. Mata-Torres, R.A. Escobar, Materials corrosion for thermal energy storage systems in concentrated solar power plants, Ren. Sust. Energy Rev. 86 (2018) 22–44, https://doi.org/10.1016/j.rser.2018.01.010.

[11] D. Nissen, D. Meeker, Nitrate-nitrite chemistry in $NaNO_3$-KNO_3 melts, Inorg. Chem. 22 (1983) 716–721, https://doi.org/10.1021/ic00147a004.

[12] F. Paniccia, P.G. Zambonin, Thermodynamics of the systems $NO_3^- = NO_2^+ + \frac{1}{2}O_2$ and $NO_3^- + \frac{1}{2}O_2 + 2e^- = NO_2^- + O_2^-$ in molten alkali nitrates, J. Chem. Soc., Faraday Trans. 1: Physical Chemistry in Condensed Phases 72 (1976) 1512–1518, https://doi.org/10.1039/F19767201512.

[13] B.D. Bond, P.W.M. Jacobs, The thermal decomposition of sodium nitrate, J. Chem. Soc. A: Inorg. Phys. Theor. Issue (0) (1966) 1265–1268, https://doi.org/10.1039/j19660001265.

[14] E.S. Freeman, The kinetics of the thermal decomposition of potassium nitrate and of the reaction between potassium nitrite and oxygen, J. Am. Chem. Soc. 79 (1957) 838–842, https://doi.org/10.1021/ja01561a015.

[15] E.S. Freeman, The kinetics of the thermal decomposition of sodium nitrate and of the reaction between sodium nitrite and oxygen, J. Phys. Chem. 60 (1956) 1487–1493, https://doi.org/10.1021/j150545a005.

[16] Y. Hoshino, T. Utsunomiya, O. Abe, The thermal decomposition of sodium nitrate and the effects of several oxides on the decomposition, Bull. Chem. Soc. Jpn. 54 (1981) 1385–1391, https://doi.org/10.1246/bcsj.54.1385.

[17] V.A. Sötz, Chemical Equilibria and Intrinsic Kinetics of Reactions in Molten Nitrate Salt, PhD Thesis, University of Stuttgart, Germany, 2021.

[18] V.A. Sötz, A. Bonk, T. Bauer, With a view to elevated operating temperatures in thermal energy storage - reaction chemistry of Solar Salt up to 630 °C, Sol. Energy Mater. Sol. Cells 212 (2020) 110577, https://doi.org/10.1016/j.solmat.2020.110577.

[19] J.W. Slusser, J.B. Titcomb, M.T. Heffelfinger, B.R. Dunbobbin, Corrosion in molten nitrate-nitrite salts, JOM 37 (1985) 24–27, https://doi.org/10.1007/BF03259692.

[20] A. Kruizenga, D. Gill, M. LaFord, Materials Corrosion of High Temperature Alloys Immersed in 600 °C Binary Nitrate Salt, Sandia National Laboratories, 2013. Report No. SAND 2013-2526.

[21] R.W. Bradshaw, S.H. Goods, Corrosion of Alloys and Metals by Molten Nitrates, Sandia National Laboratories, 2001. Report No. SAND2000-8727.

[22] S.H. Goods, R.W. Bradshaw, Corrosion of stainless steels and carbon steel by molten mixtures of commercial nitrate salts, J. Mater. Eng. Perform. 13 (2004) 78–87, https://doi.org/10.1361/10599490417542.

[23] M. Spiegel, P. Schraven, Corrosion of austenitic steels and nickel alloys in molten KNO_3–$NaNO_3$ at different temperatures: role of alloying elements, Oxid. Met. 96 (2021) 145–155, https://doi.org/10.1007/s11085-021-10063-6.

[24] M. Elbakhshwan, D.H. Lee, M. Anderson, Corrosion resistance of high nickel alloys in solar salt at 600 °C for up to 4000 h, Sol. Energy Mater. Sol. Cells 245 (2022) 111837, https://doi.org/10.1016/j.solmat.2022.111837.

[25] A.G. Fernandez, L.F. Cabeza, Molten salt corrosion mechanisms of nitrate based thermal energy storage materials for concentrated solar power plants: a review, Sol. Energy Mater. Sol. Cells 194 (2019) 160–165, https://doi.org/10.1016/j.solmat.2019.02.012.

[26] T. Meißner, C. Oskay, A. Bonk, B. Gregoire, A. Donchev, A. Solimani, M. Galetz, Improving the corrosion resistance of ferritic-martensitic steels at 600 °C in molten solar salt via diffusion coatings, Sol. Energy Mater. Sol. Cells (2021) 277.

[27] A. Bonk, W. Ding, A. Hanke, M. Braun, J. Müller, S. Klein, T. Bauer, Effect of gas management on corrosion resistance in molten solar salt up to 620 °C: corrosion of SS316-types and SS347, Corros. Sci. 227 (2024) 111700, https://doi.org/10.1016/j.corsci.2023.111700.

[28] S. Kunkel, F. Klasing, A. Hanke, T. Bauer, A. Bonk, Concentrating solar power at higher limits: first studies on molten nitrate salts at 600 °C in a 100 kg-scale hot tank, Sol. Energy Mater. Sol. Cells 258 (2023) 112412, https://doi.org/10.1016/j.solmat.2023.112412.

[29] S. Kumar, A. Hanke, A. Bonk, T. Bauer, Influence of atmosphere and austenitic stainless steel on the solar salt corrosivity, Heliyon 10 (2024) e25966, https://doi.org/10.1016/j.heliyon.2024.e25966.

[30] A. Bonk, D. Rückle, S. Kaesche, M. Braun, T. Bauer, Impact of Solar Salt aging on corrosion of martensitic and austenitic steel for concentrating solar power plants,

Sol. Energy Mater. Sol. Cells 203 (2019) 110162, https://doi.org/10.1016/j.solmat.2019.110162, 110162.
[31] J. Steinbrecher, A. Bonk, V.A. Sötz, T. Bauer, Investigation of regeneration mechanisms of aged solar salt, Materials 14 (2021) 5664, https://doi.org/10.3390/ma14195664.
[32] K. Federsel, J. Wortmann, M. Ladenberger, High-temperature and corrosion behavior of nitrate nitrite molten salt mixtures regarding their application in concentrating solar power plants. Proceedings of the SolarPACES 2014 conference, Energy Proc. 69 (2015) 618–625, https://doi.org/10.1016/j.egypro.2015.03.071.
[33] A. Le Bail, Whole powder pattern decomposition methods and applications: a retrospection, Powder Diffr. 20 (4) (2005) 316–326, https://doi.org/10.1154/1.2135315.
[34] A.A. Coelho, TOPAS and TOPAS-Academic: an optimization program integrating computer algebra and crystallographic objects written in C++, J. Appl. Cryst. 51 (2018) 210–218, https://doi.org/10.1107/S1600576718000183.
[35] D. Young, High Temperature Oxidation and Corrosion of Metals, first ed., Elsevier, 2008.
[36] https://next-gen.materialsproject.org/materials/mp-19359. (Accessed 19 March 2024).
[37] https://next-gen.materialsproject.org/materials/mp-19306. (Accessed 19 March 2024).
[38] https://next-gen.materialsproject.org/materials/mp-568345. (Accessed 19 March 2024).
[39] S. Bell, M. Sarvghad, T.-C. Ong, D. Naylor, X. Wang, Y. Yin, R. Rumman, G. Andersson, G. Will, D.A. Lewis, T. Steinberg, Corrosion of iron–nickel–chromium alloys in high temperature carbonate salt under argon atmosphere, Sol. Energy Mater. Sol. Cells 256 (2023) 112317, https://doi.org/10.1016/j.solmat.2023.112317.
[40] Bin Jenn Shaiu, P.C.S. Wu, P. Chiotti, Thermodynamic properties of the double oxides of Na_2O with the oxides of Cr, Ni and Fe, J. Nucl. Mater. 67 (1977) 13–23, https://doi.org/10.1016/0022-3115(77)90157-X.
[41] S. Bell, T. Steinberg, G. Will, Corrosion mechanisms in molten salt thermal energy storage for concentrating solar power, Renew. Sustain. Energy Rev. 114 (2019) 109328, https://doi.org/10.1016/j.rser.2019.109328.
[42] B. Liu, X. Wei, W. Wang, J. Lu, J. Ding, Corrosion behavior of Ni-based alloys in molten NaCl-$CaCl_2$-$MgCl_2$ eutectic salt for concentrating solar power, Sol. Energy Mater. Sol. Cells 170 (2017) 77–86, https://doi.org/10.1016/j.solmat.2017.05.050.
[43] Y.X. Xu, Y.L. Wang, C.L. Zeng, Electrochemical studies of the corrosion of pure Fe, Ni and Cr in molten (Li,Na,K)F, High Temp. Mater. Proc. 33 (3) (2014) 269–276, https://doi.org/10.1515/htmp-2013-0071.
[44] H.L. Chan, E. Romanovskaia, J. Qiu, P. Hosemann, J.R. Scully, Insights on the corrosion thermodynamics of chromium in molten LiF-NaF-KF eutectic salts, npj Mater. Degrad. 46 (2022), https://doi.org/10.1038/s41529-022-00251-3.
[45] S. Swaminathan, K. Sun, G.S. Was, Decoupling the roles of grain boundary oxidation and stress in IASCC of neutron-irradiated 304L stainless steel, J. Nucl. Mater. 585 (2023) 154604, https://doi.org/10.1016/j.jnucmat.2023.154604.
[46] G.S. Was, C.-B. Bahn, J. Busby, B. Cui, D. Farkas, M. Gussev, M. Rigen He, J. Hesterberg, Z. Jiao, D. Johnson, W. Kuang, M. McMurtrey, I. Robertson, A. Sinjlawi, M. Song, K. Stephenson, K. Sun, S. Swaminathan, M. Wang, E. West, How irradiation promotes intergranular stress corrosion crack initiation, Prog. Mater. Sci. 143 (2024) 101255, https://doi.org/10.1016/j.pmatsci.2024.101255.
[47] B.J. Brough, D.H. Kerridge, S.A. Tariq, Molten lithium-potassium nitrate eutectic: the reactions of some compounds of chromium, Inorg. Chim. Acta. 1 (1967) 267–270, https://doi.org/10.1016/S0020-1693(00)93183-9.
[48] J. Steinbrecher, A. Hanke, M. Braun, T. Bauer, A. Bonk, Stabilization of Solar Salt at 650 °C – thermodynamics and practical implications for thermal energy storage systems, Sol. Energy Mater. Sol. Cells 258 (2023) 112411, https://doi.org/10.1016/j.solmat.2023.112411.
[49] Y. Wang, J. Huang, H. Liu, L. Yang, C. Zeng, Effect of chlorides and sulfates on the corrosion of SS347 and GH3539 in molten solar salt at 600 °C, Sol. Energy Mater. Sol. Cells 270 (2024) 112820, https://doi.org/10.1016/j.solmat.2024.112820.
[50] D.H. Kerridge, Recent advances in molten salts as reaction media, Pure Appl. Chem. 41 (1975) 355–371, https://doi.org/10.1351/pac197541030355.
[51] P.G. Zambonin, J. Jordan, Chemistry of electron transfer and oxygen transfer in fused salts, J. Am. Chem. Soc. 89 (1967) 6365–6366. https://pubs.acs.org/doi/10.1021/ja01000a075.